Lima, P. M., Erlhagen, W., Kulikova, M. V., & Kulikov, G. Y. (2022).
Numerical solution of the stochastic neural field equation with applications to working memory.
Physica A: Statistical Mechanics and its Applications, 596, 127166.
DOI: 10.1016/j.physa.2022.127166

Numerical Solution of the Stochastic Neural Field Equation with Applications to Working Memory

P. M. Lima[a,*], W. Erlhagen[b], M. V. Kulikova[a], G. Yu. Kulikov[a]

[a] *CEMAT, Instituto Superior Técnico, Universidade de Lisboa, Av. Rovisco Pais, 1049-001 Lisboa, Portugal.*
[b] *Centro de Matemática, Universidade do Minho, Guimaraes, Portugal.*

Abstract

The main goal of the present work is to investigate the effect of noise in some neural fields, used to simulate working memory processes. The underlying mathematical model is a stochastic integro-differential equation. In order to approximate this equation we apply a numerical scheme which uses the Galerkin method for the space discretization. In this way we obtain a system of stochastic differential equations, which are then approximated in two different ways, using the Euler-Maruyama and the Itô-Taylor methods. We apply this numerical scheme to explain how a population of cortical neurons may encode in its firing pattern simultaneously the nature and time of sequential stimulus events. Numerical examples are presented and their results are discussed.

Keywords: Stochastic neural field equation, Galerkin method, one- and multi-bump solutions.
2000 MSC: 35R60, 60H15, 60H20, 65C20, 65R20, 65Z05, 92C20, 93C23

1. Introduction

Dynamic Neural Fields (DNFs) have been introduced in the 1970s as simplified mathematical models of pattern formation in neural tissue in which the interaction of billions of neurons is treated as a continuum [1], [35]. These models take the form of a nonlinear integro-differential equation

$$\frac{\partial}{\partial t}U(\mathbf{x_1},t) = I(\mathbf{x_1},t) - \alpha U(\mathbf{x_1},t) + \int_\Omega F(\|\mathbf{x_1}-\mathbf{x_2}\|_2)S(U(\mathbf{x_2},t))d\mathbf{x_2}, \tag{1}$$

$$t\in[0,T], \quad \mathbf{x_1},\mathbf{x_2}\in\Omega\subset\mathbb{R}^2,$$

where

- vectors $\mathbf{x_1}$ and $\mathbf{x_2}$ denote points in the plane, each of them has two coordinates (x, y);
- $U(\mathbf{x_1}, t)$ (the unknown function) denotes the membrane potential at the position $\mathbf{x_1}$ and time t; for a certain t_0 , $U(\mathbf{x_1}, t_0)$ represents the spatial distribution of the membrane potential on the domain Ω. In the context of our paper, this function usually displays a certain number of *bumps* or *activity domains*, that is, regions where U is greater than a certain threshold value meaning that the neurons in these regions are spiking with higher intensity.

*Corresponding author.
Email addresses: pedro.t.lima@ist.utl.pt (P. M. Lima), Wolfram.erlhagen@math.uminho.pt (W. Erlhagen), maria.kulikova@ist.utl.pt (M. V. Kulikova), gkulikov@tecnico.ulisboa.pt (G. Yu. Kulikov)

- $I(\mathbf{x_1}, t)$ represents the external sources of excitation. In the examples we are concerned with, I can be regarded for example as a visual stimulus extended in time; therefore $I(\mathbf{x_1}, t)$ represents the intensity of a certain color of the signal at time t (for a detailed explanation, see Sec. 2).

- $\alpha > 0$ is the potential decay rate (it reflects the potential dissipation in the absence of external input or neuron interaction).

- S is the dependence between the firing rate of the neurons and their membrane potentials. Typically $S = 0$ if the potential is lower a certain threshold b; for $V > \theta$ it varies monotonically between 0 and 1. In our examples, we consider the simplest case, when S is the Heaviside function ($S(V) = 1$ for $V > b$ and $S(V) = 0$ otherwise).

- $F(\|\mathbf{x_1} - \mathbf{x_2}\|_2)$ is the connectivity function describing the coupling strength between any two neurons at the positions $\mathbf{x_1}$ and $\mathbf{x_2}$, which is assumed to depend on their distance, only.

When solving equation (1) one usually searches for a function U satisfying an initial condition of the form $U(\mathbf{x}, 0) = U_0(\mathbf{x})$ where $\mathbf{x} \in \Omega$ and U_0 is a given real function. In this article, we assume that Ω is a rectangle.

To support the existence of stable multi-bump solutions, the connectivity function F in (1) is chosen to be of oscillatory type with several zero crossings. They define the distances where excitation or inhibition dominates [9, 20].

Dynamic field theory is still a very active area of multidisciplinary research since the level of abstraction and complexity of DNFs has been proven to be adequate to explain many aspects of cortical information processing and to push a deeper mathematical understanding of their behavior. Two recent books, namely, *Neural Fields* [3] and *Dynamic Thinking* [32], give an excellent overview of current research topics in the mathematical analysis of neural field equations and in applications of DNFs to the areas of neuroscience and robotics.

Although the numerical implementation of a DNF can be seen as a Recurrent Neural Network (RNN) with a specific coupling function, it is important to stress the difference to popular RNN-based approaches to learning sequential data (for a recent review see [34]). While in DNF models persistent neural population activity represents the basic unit of learning and representation, information processing in RNN models is based on adjustable synaptic weights which are trained by large amount of data.

The non-local nature of DNFs has led to the development of a set of analytical and numerical tools for studying spatiotemporal patterns, based around natural extensions of those used for local differential equations. A majority of such research is dedicated to the existence, uniqueness and stability of localized activity patterns (or bumps) and traveling pulses in one spatial dimension. In [1], Amari finds bump solutions that are bistable with a homogeneous state in a model with a Heaviside nonlinearity and a symmetric interaction kernel of lateral inhibition type (short range excitation – long range inhibition). He performs a linear stability analysis by calculating the effect of perturbations on the bump boundaries. Another mathematical work focuses on geometric singular perturbation analysis as well as numerical bifurcation techniques for analyzing such solutions [30], [11]. A rigorous nonlinear stability analysis of traveling pulse solutions is fulfilled using an Evans function approach [31]. Multi-bump solutions are also studied by transforming the integro-differential equation into a corresponding fourth-order PDE with an appropriately chosen connectivity kernel. Then a search for bifurcations from single-bump solutions is fulfilled. That

approach evidences that N-bump solutions can occur when the lateral inhibition is modulated by a spatially oscillating component [20].

A comparably little mathematical work has been devoted to DNFs with external inputs so far. From an application point of view, not only the existence of an attractor state like a N-bump solution matters but also a better understanding of how the evolution of such patterns depends on the distribution of external drives and on non-homogeneous initial states is of highest interest. With the application of a working memory function in mind, rigorous conditions are recently studied on the spatial distribution of N localized, transient inputs that may switch from a resting state to a stable N-bump solution representing a multi-item memory of stimulus events. The analysis includes the finding of fixed points of a system of N coupled ODEs describing the motion of weakly interacting bumps [9].

There exist a few studies that extend analytical results on bump solutions to 2D fields. The PDE method is used for investigating specific kernels symmetry breaking of rotationally symmetric bumps and the formation of multi-bump solutions [21]. A later work fulfilled by means of Fourier techniques shows that non-radially symmetric perturbations can destabilize bumps to a rich set of possible patterns existing in 2D fields [2].

The mathematical modeling of working memory using neural fields has been the subject of recent research. In particular, in [36], the authors introduce a new bump attractor model in which the bump width and amplitude not only reflect qualitative and quantitative characteristics of a preceding input but also the continuous integration of evidence over longer timescales. Some applications of this new model to robotics have been investigated in [37] and [38].

Numerical simulations are widely used as a complementary tool to study neural field models. The choice of a sufficiently small discretization step size increases the computational cost of the spatial convolution which challenges in particular the use of 2D fields in, for instance, robotics applications that require real-time performance. In the last years, special attention is paid to the creation of effective numerical algorithms for Neural Field Equations (NFEs), specially in the 2D setting [8, 12, 13]. The new algorithm proposed in [23] drastically improves the efficiency of the computations by using interpolation techniques, which allow a strong reduction of the size of matrices, while preserving the accuracy of the outcome results.

The treatment of stochastic one-dimensional DNF models is a relatively new research topic. Of a particular interest is studying the impact of additive or multiplicative noise on specific solutions like, for instance, bumps of the deterministic NFE. Due to the assumed translation symmetry of the spatial interactions, bumps do not remain fixed at certain positions but tend to wander along the spatial domain in a purely diffusive way [14] . In [16], a stochastic version of the neural field equation (1) with additive noise is introduced as follows:

$$dU(\mathbf{x_1},t) = \left(I(\mathbf{x_1},t) - \alpha U(\mathbf{x_1},t) + \int_\Omega F(\|\mathbf{x_1}-\mathbf{x_2}\|_2) S(U(\mathbf{x_2}),t) d\mathbf{x_2} \right) dt + \epsilon dW(\mathbf{x_1},t), \qquad (2)$$

where $t \in [0,T]$, $\mathbf{x_1} = (x,y) \in \Omega \subset \mathbb{R}^2$, $W(\mathbf{x_1},t)$ is a Q-Wiener process. The initial condition $U_0(\mathbf{x_1}) = U(\mathbf{x_1},0)$ is supposed to satisfy the periodic boundary conditions in space $\mathbf{x_1} \in \mathbb{R}^2$.

In [17], a numerical algorithm is proposed for integrating the stochastic NFE (2) and some evidence is reported for confirming its accuracy and efficiency. This algorithm is then extended to the case of two spacial dimensions, which enables for simulating the effect of noise on multi-bump solutions in 2D neural fields [18].

Below, we present our numerical investigation of a stochastic 2D neural field equation, which analyzes and explains how a population of cortical neurons may encode in its firing pattern the

nature and time of sequential stimulus events, simultaneously. Moreover, we study how noise-induced perturbations may affect the coding process. The novelty of this contribution is the use of a new algorithm based on the Itô-Taylor approximation of stochastic differential equations, which enables the significantly-improved accuracy of stochastic simulations (in comparison with those obtained in [18], for example). This allows some new problems related with working memory and its perturbation under the effect of noise to be investigated numerically .

The rest of this paper has the following structure. In section 2, we analyze the application of dynamic neural fields to the mathematical modeling of working memory. In section 3, we present two numerical algorithms of different convergence order for approximation of 2D stochastic neural fields. In particular, the first method is based on the Euler-Maruyama discretization, whereas the second one is rooted in the Itô-Taylor approximation. Results of numerical simulations are presented in section 4, where their physical interpretation is also discussed. We conclude our paper with some outcome remarks placed in section 5.

2. Application of Dynamic Neural Fields to Working Memory

Working memory (WM) defined as the ability to actively retain stimulus information over short periods of time is crucial for cognitive control of behavior. Persistent, stimulus-selective activity observed in many brain areas is commonly believed to represent a neural substrate of WM [5]. Neural field models explain the emergence of stable representations of continuous-valued information such as object color or movement direction by assuming a distance-dependent neural connectivity pattern in feature space. The WM function is implemented in a bi-stable regime of the field dynamics. A brief localized input may switch the neural activity from a homogeneous resting state below threshold to a localized, suprathreshold activation pattern (or bump) which becomes self-sustained due to the recurrent interactions in the network. The peak position of the bump encodes a specific value of the continuous input dimension. In other words, when using equation (1) to model working memory, we aim at describing the neural population response to specific inputs. Both the average level of activity $U(x_1, t)$ (voltage) and the input intensity $I(x_1, t)$ are functions of time, t, and position, x_1, in feature space. Fig. 1 shows an example of a bump in a one-dimensional field encoding a specific hue value of the color dimension. When two or more transient inputs are applied simultaneously or sequentially at different field positions, a multi-bump pattern stabilizes representing a multi-item memory.

Fig. 2 illustrates the formation of a two-bump pattern in response to two simultaneously acting inputs. Notice that the population activity decays slightly after the cessation of the inputs, but the recurrent interactions are strong enough to maintain the pattern above the threshold.
The 2D-field model of serial order of sequential events adds a temporal dimension (x) to the color dimension (y)[1]. This choice is motivated by the experimental observation of neurons that are tuned to the temporal intervals and/or the ordinal structure of sequential tasks [26]. We use a traveling wave (assumed to be triggered by a sequence onset signal) as a second input to the field for integrating the information about the event timing relative to the sequence onset. Traveling waves, which are observed in many cortical areas, provide a subthreshold depolarization to individual neurons and increase their firing probability in the presence of external stimuli [29]. Consisting with this view, we suppose that only at field positions being forced by the traveling wave

[1]When describing the working memory problems the coordinates are given by the vector $\mathbf{x_1} = (x, y)$

and the color input, simultaneously, the combined input is strong enough to trigger the evolution of a bump. Projections of the bump onto the x and y axes reveal bell-shaped activity profiles, which are consistent with the notion of broadly tuned neurons in the feature (color) dimension and the time dimension [6, 26]. Figs. 3 and 4 illustrate the localized input and the wave input to the 2D-field, respectively. If a signal of color y occurs at a certain time, we will have a ridge-like input, which is localized in the feature space y but extends in the time dimension x. The wave has the form of a ridge that extends in the y direction and propagates in the direction of x within the elapsed time t since the sequence onset occurred at $t = 0$. A single bump evolves in response to the combined input (see Fig. 5) and still persists when all inputs have been switched off (see Fig. 6). The details of this mechanism will become more clear while considering specific examples in Sec. 5.

In our numerical simulations, we examine the robustness of a dynamic neural field model of serial order in the presence of additive noise in an experiment in which a sequence of color cues acts. The two-dimensional field model in use implements the idea that the serial order of stimulus events can be represented in terms of their location along the feature dimension and the temporal one. The position of each individual bump of the evolving multibump encodes the memory of a specific color cue acting at a specific time instant after the sequence onset. Importantly, the joint cue-timing representation allows us to address the problem of cue repetitions, which has been identified as a major challenge for models of serial order [10].

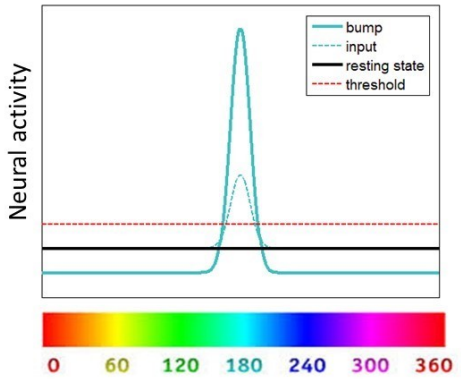

Figure 1: Stable bump triggered by a single color stimulus

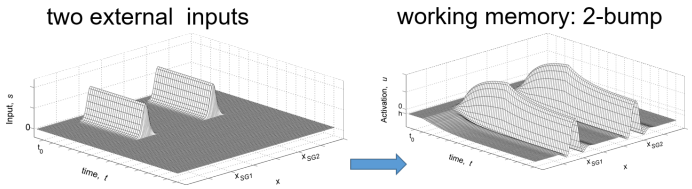

Figure 2: External stimuli and their representations in working memory

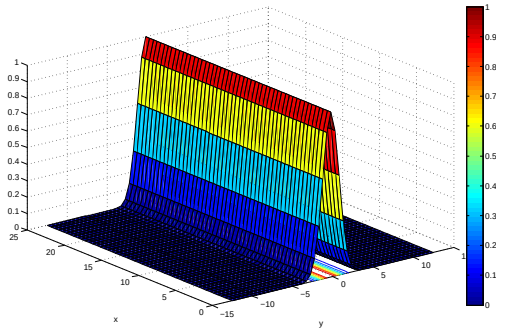

Figure 3: Surface graph of the input function corresponding to a light signal of the color $y = 0$

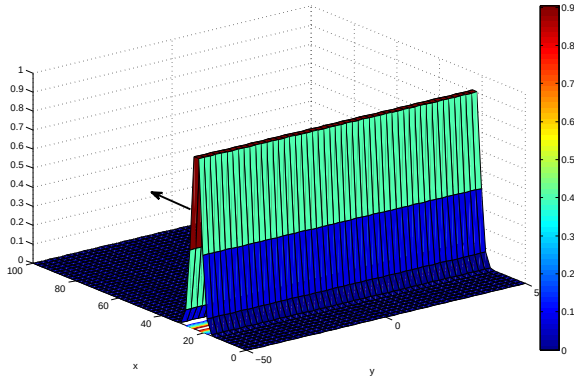

Figure 4: Input function corresponding to a traveling wave, moving in the direction of the x axis

3. Numerical methods for solving stochastic neural field Equations

Since NFEs cannot be solved analytically in general, numerical methods for their approximate solution have been developed by many researchers. In [8], a computational method of such sort is introduced. It applies a quadrature rule in space for reducing the problem to a system of delay differential equations, which is then solved by a standard algorithm for this kind of equations. A more efficient approach is proposed in [12, 13], where the authors introduce a new algorithm to deal with the convolution kernel of the equation and use the Fast Fourier Transforms to reduce significantly the computational effort required by numerical integration. Recently, a new numerical method for the approximation of two-dimensional neural fields is also presented. It uses an implicit second order scheme for the integration in time and applies the Chebyshev interpolation for reducing the dimensions of the matrices arisen [23]. Some applications of this algorithm to neuroscience problems are discussed in [24]. In the stochastic case, the numerical approximation of NFE becomes a harder challenge. Numerical algorithms for the stochastic NFE are proposed in [17–19, 25].

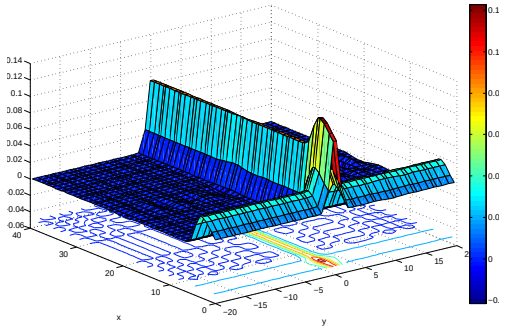

Figure 5: Combination of two inputs generating a bump state

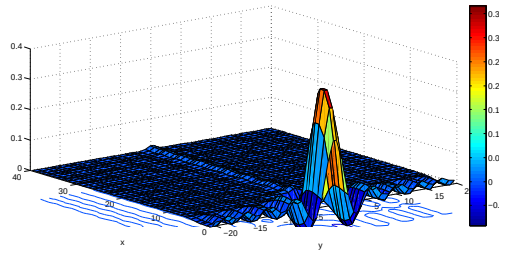

Figure 6: Example of a stable bump solution which remains after all the inputs have been switched off

3.1. Spectral approximation: Galerkin-type approach

The numerical integration scheme employed in the present work is based on the Karhunen-Loève presentation of the solution to the 2D-stochastic NFE (2D-SNFE) in the following form:

$$U(\mathbf{x_1},t)=\sum_{k=0}^{\infty}\sum_{l=0}^{\infty}u_{kl}(t)v_{kl}(\mathbf{x_1}) \tag{3}$$

where $v_{kl}(\mathbf{x_1})$ stand for the eigenfunctions of the covariance operator of the noise term in the 2D-SNFE model (2) and $u_{kl}(t)$ are the corresponding coefficient random processes. The set of such functions $\{v_{kl}(\mathbf{x_1})\}$ in equation (3) establishes an orthonormal basis in the Hilbert space associated with the problem at hand.

Next, the deterministic continuous-in-space factors $v_{kl}(\mathbf{x_1})$ are defined on the square domain $\Omega=[-L,L]\times[-L,L]$ of real numbers by satisfying the formula

$$v_{kl}(\mathbf{x_1}):=\begin{cases}\dfrac{1}{2L}, & \text{if } k=0,\ l=0,\\ \dfrac{1}{\sqrt{2}L}\cos(k\pi x/L), & \text{if } k\geq 1,\ l=0,\\ \dfrac{1}{\sqrt{2}L}\cos(l\pi y/L), & \text{if } k=0,\ l\geq 1,\\ \dfrac{1}{L}\cos(k\pi x/L)\cos(l\pi y/L), & \text{if } k\geq 1,\ l\geq 1.\end{cases} \tag{4}$$

The formulas for evolution of the stochastic processes $u_{kl}(t)$ in time are derived in [18]. More precisely, we take into account that the functions $\{v_{kl}(\mathbf{x_1})\}$ in use establish an orthonormal basis and yield, for evolving the uncorrelated processes $u_{kl}(t)$, determined on the interval $[0,T]$, the following multivariate stochastic differential equation:

$$du_{kl}(t)=\Big[\big\langle I(\mathbf{x_1},t),v_{kl}(\mathbf{x_1})\big\rangle-\alpha u_{kl}(t)+FS_{kl}\big(U(\mathbf{x_1},t)\big)\Big]dt+\varepsilon\lambda_{kl}d\beta_{kl}(t) \tag{5}$$

where the nonlinear term refers to the double integral, that is,

$$FS_{kl}\big(U(\mathbf{x_1},t)\big):=\int_{\Omega}v_{kl}(\mathbf{x_1})\left[\int_{\Omega}F\big(\|\mathbf{x_1}-\mathbf{x_2}\|_2\big)S\Big(\sum_{n=0}^{\infty}\sum_{m=0}^{\infty}u_{nm}\big(t\big)v_{nm}(\mathbf{x_2})\Big)d\mathbf{x_2}\right]d\mathbf{x_1}, \tag{6}$$

and the inner product in SDE (5) enjoys the standard definition

$$\big\langle I(\mathbf{x_1},t),v_{kl}(\mathbf{x_1})\big\rangle:=\int_{\Omega}I(\mathbf{x_1},t)v_{kl}(\mathbf{x_1})\,d\mathbf{x_1} \tag{7}$$

in the square space domain $\Omega\equiv[-L,L]\times[-L,L]\subset\mathbb{R}^2$ under consideration, at any time t. Finally, the scalars λ_{kl} and the stochastic process increments $d\beta_{kl}(t)$ come from the infinite series representation of the differential $dW(\mathbf{x_1},t)$ of the trace-class space-valued Q-Wiener process in 2D-SNFE (2). It is known that the mentioned representation has the following form:

$$dW(\mathbf{x_1},t)=\sum_{k=0}^{\infty}\sum_{l=0}^{\infty}v_{kl}(\mathbf{x_1})\lambda_{kl}d\beta_{kl}(t) \tag{8}$$

with the stochastic processes $\beta_{kl}(t)$ being the mutually independent Brownian motions with zero mean and unit variance and λ_{kl} standing for the eigenvalues of the covariance operator Q. The correlation in this noise obeys the conventional formula

$$\mathbf{E}\{W(\mathbf{x_1},t)W(\mathbf{x_2},s)\} = \min\{t,s\}\frac{1}{2\xi}\exp\left(\frac{-\pi\|\mathbf{x_1}-\mathbf{x_2}\|_2^2}{4\xi^2}\right)$$

for any space points $\mathbf{x_1}, \mathbf{x_2} \in \Omega$ and time instants $t, s > 0$. Here and below, $\mathbf{E}\{\cdot\}$ refers to the expectation operator, and the fixed parameter ξ determines the spatial correlation length. Following [33], we impose the condition $\xi << 2L$ and, then, yield explicitly values of the eigenvalues λ_{kl} of the covariance operator Q in series (8). These are defined as follows:

$$\lambda_{kl} = \sqrt{\exp\bigl(-\xi^2(k^2+l^2)/(4\pi)\bigr)}. \tag{9}$$

The Galerkin-type approximation underlying the numerical scheme in use implies that the infinite series (3) is truncated to a finite summation formula. We choose a sufficiently large positive integer K and replace the exact solution (3) to 2D-SNFE (2) with its approximation of the fashion

$$U_K(\mathbf{x_1},t) := \sum_{k=0}^{K}\sum_{l=0}^{K} u_{kl}(t)v_{kl}(\mathbf{x_1}) \tag{10}$$

where the deterministic functions $v_{kl}(\mathbf{x_1})$ are assigned by rule (4) and the stochastic processes $u_{kl}(t)$ satisfy the SDE given by formula (5).

We introduce then an equidistant mesh in the domain Ω with the step sizes $h_x = h_y = 2L/N$, where N is a number of the subdivision steps fulfilled in each direction of the square domain $x \times y = [-L, L] \times [-L, L]$. More precisely, the mesh $\mathbf{X}$ consists of 2D-vectors in the domain Ω, that is, $\mathbf{X}$ is the square matrix of size $N+1$ whose (i,j)th entry is the vector with the coordinates $x^i = x^0 + ih_x$ and $y^j = y^0 + jh_y$. We recall that the number of summation terms in the approximate solution (10) and that of the discretization steps used in the domain Ω must obey the condition $N >> K$, which is explained in [18].

The last step in deriving the set of equations to be solved is to substitute the Galerkin-type solution (10) into SDE (5) and replace the continuous space-dependent functions in formulas (5) and (6) with their values calculated at nodes of the mesh $\mathbf{x}$ introduced. We also approximate the integrals appeared in the 2D-SNFEs under study by means of the Trapezoidal Rule summations, as follows:

$$\langle I(\mathbf{x_1},t), v_{kl}(\mathbf{x_1})\rangle \approx h_x h_y \sum_{i=0}^{N-1}\sum_{j=0}^{N-1} I\bigl(x^i,y^j,t\bigr)v_{kl}\bigl(x^i,y^j\bigr), \tag{11}$$

$$\begin{aligned} FS_{kl}\bigl(U(\mathbf{x_1},t)\bigr) \;\approx\; & (h_x h_y)^2 \sum_{i=0}^{N-1}\sum_{j=0}^{N-1} v_{kl}\bigl(x^i,y^j\bigr)\Biggl[\sum_{p=0}^{N-1}\sum_{q=0}^{N-1} F\Bigl(\Bigl\|\begin{bmatrix} x^i - x^p \\ y^j - y^q\end{bmatrix}\Bigr\|_2\Bigr) \\ & \times\; S\Bigl(\sum_{n=0}^{K}\sum_{m=0}^{K} u_{nm}(t)v_{nm}\bigl(x^p,y^q\bigr)\Bigr)\Biggr]. \end{aligned} \tag{12}$$

In [18], the effective MATLAB-based solution technique has been presented. At first we vectorize all values and functions defined at entries of the space-discterized-mesh-matrix $\mathbf{X}$ by using

MATLAB command `reshape` and convert any matrix into the requested vectorized form. For instance, the mesh $\mathbf{X}$ is translated into its column-wise vector representation by the command $\mathbf{X}(:)$. We note that formulas (11) and (12) imply that the last row and column of the mesh array $\mathbf{X}$ are not used and must be excluded from the calculation, as explained in the cited paper. That is why we further remove them from our mesh. This entails that the (i,j)th entry of such a truncated matrix $\mathbf{X}$ and the $(j\times N+i+1)$th entry in its vectorized representation $\mathbf{X}(:)$ coincide. Then, we vectorize the scalar stochastic processes $u_{kl}(t)$ in SDE (5) to the fashion

$$\mathbf{u}(t) := \big[u_{00}(t), u_{01}(t), \ldots, u_{0K}(t), u_{10}(t), u_{11}(t), \ldots, u_{1K}(t), \ldots, u_{K0}(t), u_{K1}(t), \ldots, u_{KK}(t)\big]^\top.$$

We recall that the random-disturbance-vector $d\mathbf{W}$ is the multivariate zero-mean white Gaussian process with the diagonal covariance, whose nonzero entries come from formula (9) and are sorted in the same way as the entries $u_{kl}(t)$ above, i.e. $[\lambda_{00}^2, \lambda_{01}^2, ..., \lambda_{0K}^2, \lambda_{10}^2, \lambda_{11}^2, ..., \lambda_{0K}^2, \ldots, \lambda_{K0}^2, \lambda_{K1}^2, ..., \lambda_{KK}^2]$.

Similarly, we reshape and vectorize all the Fourier-basis-functions (4) evaluated at nodes of our truncated space mesh $\mathbf{X}$. For that, we assemble the rectangular matrix $\mathbf{V}$ of size $(K+1)^2\times N^2$ whose rows are sorted in the same manner as the stochastic processes $u_{kl}(t)$ above. More formally, every eigenfunction $v_{kl}(\mathbf{x_1})$ is calculated first at space points (x^i, y^j), $i,j = 0,1,\ldots,N-1$, in use. Second, the resulting matrix derived for the function $v_{kl}(\mathbf{X})$ evaluated at all nodes of our truncated mesh $\mathbf{X}$ is further reshaped to the requested vectorized fashion of size N^2 by the MATLAB command $v_{kl}(\mathbf{X}(:))$. Here and below, we follow the MATLAB notation in which $v_{kl}(\mathbf{X})$ refers to the $(N\times N)$-matrix whose entries are the values $v_{kl}(x^i, y^j)$, $i,j = 0,1,\ldots,N-1$. Having fulfilled the above procedure for each eigenfunction in the Fourier-basis-equations (4), we obtain a set of $(K+1)^2$ reshaped vectors $v_{1:(K+1)^2}\big(\mathbf{X}(:)\big)$ of size N^2. Eventually, the (k,l)th vector is saved in the form of the $(k\times K+l+1)$th row in the Fourier-basis-matrix $\mathbf{V}\in\mathbb{R}^{(K+1)^2\times N^2}$. In other words, the rows of such a matrix $\mathbf{V}$ are sorted in the same manner as the unknown variables $u_{kl}(t)$, that is, every row of this matrix $\mathbf{V}$ stores the values of a particular Fourier-basis-function (4) evaluated at the vectorized-truncated-space-mesh $\mathbf{X}(:)$. The above notation converts the inner product (11) to its MATLAB-oriented fashion, that is fast to execute because of the simple matrix-vector multiplication

$$\big\langle I(\mathbf{x_1},t), v_{kl}(\mathbf{x_1})\big\rangle \approx h_x h_y\, \mathbf{V}(k\times K+l+1,:)\times I(\mathbf{X}(:),t). \tag{13}$$

Eventually, with the use of formulas (11)–(13), the stochastic processes $u_k(x)$ $k=0,1,\ldots,K$, employed in the numerical solution (10) are computed by solving the vectorized SDE

$$d\mathbf{u}(t) = \big[h_x h_y \mathbf{V}\times I(\mathbf{X}(:),t) - \alpha\mathbf{u}(t) + \mathbf{FS}\big(U_K(\mathbf{X}(:),t)\big)\big]dt + \varepsilon d\mathbf{W} \tag{14}$$

where the term $\mathbf{FS}\big(U_K(\mathbf{X}(:),t)\big)$ stands for the $(K+1)^2$-dimensional column-vector with its $(k\times K+l+1)$th entry determined by equation (12). The efficient MATLAB-based implementation can be achieved by taking into account that the term $\mathbf{FS}(U_K(\mathbf{X}(:),t))$ can be efficiently computed using the formula

$$\mathbf{FS}\big(U_K(\mathbf{X}(:),t)\big) = (h_x h_y)^2\,\mathbf{V}\times\mathbf{F}\times\mathbf{s} \tag{15}$$

where the time-variant column-vector $\mathbf{s}$ is of size N^2 and, for any $i,j=0,1,\ldots,N-1$, its $(j\times N+i+1)$th entry is given by the value $S\big(\mathbf{u}^\top(t)\mathbf{V}(:,j\times N+i+1)\big)$ at each time instant t. We recall that the matrix $\mathbf{V}$ represents the values of Fourier-basis-functions (4) evaluated at the vectorized-truncated-space-mesh $\mathbf{X}(:)$, but the MATLAB command $\mathbf{V}(:,j\times N+i+1)$ returns the $(j\times N+i+1)$th column in the latter matrix. In other words, the mentioned column contains

the values of all eigenfunctions $v_{kl}(\mathbf{x_1})$, $k,l=0,1,\ldots,K$, computed at the space position (x^i,y^j). Lastly, the notation $\mathbf{F}$ refers to the symmetric matrix of size N^2 whose $(j\times N+i+1, q\times N+p+1)$-entry means the following factor in calculation (12):

$$F\Big(\Big\|\begin{bmatrix}x^i-x^p\\ y^j-y^q\end{bmatrix}\Big\|_2\Big),\quad i,j,p,q=0,1,\ldots,N-1. \tag{16}$$

Further details of the efficient implementation of formula (15) in practical simulations are explained in [18, section II].

3.2. The method of strong convergence order 0.5

Kulikova et al. [18] suggest using the Euler-Maruyama scheme [15, section 10.2] of strong convergence order 0.5 for attacking SDE (14) on some equidistant mesh predefined by the user in the time interval $[0,T]$ of 2D-SNFE (2). Assuming that the time-integration step size h_t is sufficiently small, the cited authors arrive at the discretized multivariate stochastic process

$$\mathbf{u}(t_{j+1})=\mathbf{u}(t_j)+h_t\mathbf{f}\big(\mathbf{u}(t_j),t_j\big)+\varepsilon\boldsymbol{\Lambda}^{1/2}\boldsymbol{\Delta}\mathbf{W} \tag{17}$$

with the time instants $t_j:=jh_t$, the matrix $\boldsymbol{\Lambda}^{1/2}$ being a square-root factor of the diagonal matrix $\boldsymbol{\Lambda}$, i.e. $\boldsymbol{\Lambda}=\boldsymbol{\Lambda}^{1/2}\boldsymbol{\Lambda}^{\top/2}$ and, hence, $\boldsymbol{\Lambda}^{1/2}:=\mathrm{diag}\{\lambda_{00},\lambda_{01},...,\lambda_{0K},\lambda_{10},\lambda_{11},...,\lambda_{0K},\ldots,\lambda_{K0},...,\lambda_{KK}\}$. In addition, the discretized Gaussian vector $\Delta\mathbf{W}$ of size $(K+1)^2$ is generated from the standard normal distribution $\mathcal{N}(\mathbf{0}_{(K+1)^2},h_t\mathbf{I}_{(K+1)^2})$. Finally, the drift coefficient in SDE (17) is defined as follows:

$$\mathbf{f}\big(\mathbf{u}(t_j),t_j\big):=h_xh_y\mathbf{V}\times I(\mathbf{X}(:),t_j)-\alpha\mathbf{u}(t)+\mathbf{FS}\big(U_K(\mathbf{X}(:),t_j)\big). \tag{18}$$

3.3. The method of strong convergence order 1.5

Here, we derive a more accurate numerical method based on the Itô-Taylor approximation of the strong convergence order 1.5 [15, section 10.4]. Taking into account the time-invariant fashion of the noise term in SDE (14) and following [19], we arrive at the discretized stochastic process

$$\mathbf{u}(t_{j+1})=\mathbf{u}(t_j)+h_t\mathbf{f}_d\big(\mathbf{u}(t_j),t_j\big)+\varepsilon\boldsymbol{\Lambda}^{1/2}\Delta\mathbf{W}_1+\mathbb{L}\mathbf{f}\big(\mathbf{u}(t_j),t_j\big)\Delta\mathbf{W}_2 \tag{19}$$

with the time instants $t_j:=jh_t$, the matrix $\boldsymbol{\Lambda}^{1/2}$ being a square-root factor of the diagonal matrix $\boldsymbol{\Lambda}$, i.e. $\boldsymbol{\Lambda}=\boldsymbol{\Lambda}^{1/2}\boldsymbol{\Lambda}^{\top/2}$ and, hence, $\boldsymbol{\Lambda}^{1/2}:=\mathrm{diag}\{\lambda_{00},\lambda_{01},...,\lambda_{0K},\lambda_{10},\lambda_{11},...,\lambda_{0K},\ldots,\lambda_{K0},\lambda_{K1},...,\lambda_{KK}\}$. In this case,the Itô-Taylor-discretized version of the drift coefficient has the form

$$\mathbf{f}_d\big(\mathbf{u}(t_j),t_j\big):=\mathbf{f}\big(\mathbf{u}(t_j),t_j\big)+\frac{h_t}{2}\mathbb{L}_0\mathbf{f}\big(\mathbf{u}(t_j),t_j\big) \tag{20}$$

where the function $\mathbf{f}\big(\mathbf{u}(t_j),t_j\big)$ is given by formula (18) and the differential operator $\mathbb{L}_0$ is defined as follows:

$$\mathbb{L}_0:=\frac{\partial}{\partial t}+\sum_{k=1}^{(K+1)^2}\mathbf{f}_k\frac{\partial}{\partial u_k}+\frac{\varepsilon^2}{2}\sum_{i,p,r=1}^{(K+1)^2}\boldsymbol{\Lambda}_{pi}^{1/2}\boldsymbol{\Lambda}_{ri}^{1/2}\frac{\partial^2}{\partial u_p\partial u_r}. \tag{21}$$

The factor $\mathbb{L}\mathbf{f}\big(\mathbf{u}(t_j),t_j\big)$ in approximation (19) means the matrix whose (k,i)th entry $\mathbb{L}_i\mathbf{f}_k\big(\mathbf{u}(t_j),t_j\big)$ is computed in line with the rule

$$\mathbb{L}_i:=\varepsilon\sum_{k=1}^{(K+1)^2}\boldsymbol{\Lambda}_{ki}^{1/2}\frac{\partial}{\partial x_k},\quad i=0,1,\ldots,K, \tag{22}$$

with every scalar $\mathbf{\Lambda}_{ki}^{1/2}$ refering to the (k,i)th entry in the covariance-matrix-square-root $\mathbf{\Lambda}^{1/2}$ of size $(K+1)^2$. In addition, the pair of discretized correlated Gaussian vectors $\Delta\mathbf{W}_1$ and $\Delta\mathbf{W}_2$ of size $(K+1)^2$ is generated from the pair of uncorrelated standard Gaussian vectors $\mathcal{N}_1(\mathbf{0}_{(K+1)^2}, \mathbf{I}_{(K+1)^2})$ and $\mathcal{N}_2(\mathbf{0}_{(K+1)^2}, \mathbf{I}_{(K+1)^2})$ of the same size, where $\mathbf{0}_{(K+1)^2}$ and $\mathbf{I}_{(K+1)^2}$ stand for the zero-vector and identity matrix of the size $(K+1)^2$, respectively, by the following formulas [15, section 10.4]: $\Delta\mathbf{W}_1 := h_t^{1/2}\mathcal{N}_1(\mathbf{0}_{(K+1)^2}, \mathbf{I}_{(K+1)^2})$, $\Delta\mathbf{W}_2 := h_t^{3/2}(\mathcal{N}_1(\mathbf{0}_{(K+1)^2}, \mathbf{I}_{(K+1)^2}) + \mathcal{N}_2(\mathbf{0}_{(K+1)^2}, \mathbf{I}_{(K+1)^2})/\sqrt{3})/2$.

Formulas (17)–(22) constitute two approaches for computing the coefficient functions $u_{kl}(t)$ utilized within the Galerkin-sort numerical solution (10). In the subsequent section, we apply these different order approximations for a verification of our simulation results obtained by the Euler-Maruyama scheme.

4. Numerical simulation results

The numerical simulations presented in [22] support the conjecture that if the external input has the appropriate intensity and duration, and if the connection kernel is of a certain type (see equation (23)) the neural activity can generate stable multi-bump solutions that contain the information carried by the external signals.

Here, our goal is to check how a random disturbance can affect the behavior of the solutions. In particular, how the structure of the multi-bump stationary solutions observed can respond to such random perturbations.

With this purpose in mind, we use two different order numerical algorithms described in section 3 and compare their outcomes.The discrepancy between the results obtained by the two methods gives us an estimate of the computational error associated to the lower-order computational technique.

In all the examples considered in this section, the connectivity kernel F is of oscillating type

$$F(r) = A\exp(-lr)\,(l\sin(a_1 r) + \cos(a_1 r)) \tag{23}$$

where A, a_1, l are certain positive constants (see [22]).

The activation function S is of the Heaviside kind:

$$S(U) = H(U-b),$$

where $b > 0$ is a certain threshold.

The function I represents the sum of the external inputs, that is, has the form:

$$I(x,y,t) = \sum_{i=0}^{n} I_i(x,y,t),$$

where I_0 is a traveling wave of the fashion

$$I_0(x,y,t) = \alpha_0\exp(-\gamma_0(x-vt)^2) \tag{24}$$

with $0 \le t \le T$, $(x,y) \in [-L,L]\times[-L,L]$, $v > 0$ being the propagation speed of the traveling wave. The remaining inputs are localized (with their peaks at points C_i):

$$I_i(x,y,t) = \alpha_i\exp\left(-\gamma_i(y-C_i)^2\right) \tag{25}$$

t	$\|E\|_\infty$	$\|U\|_\infty$	$\|E\|_2$	$\|U\|_2$
0.5	0.0056	0.0916	0.045	0.9307
2.5	0.0321	0.2444	0.1706	1.3024

Table 1: Error norms in Example 1, deterministic case

t	$\|E\|_\infty$	$\|E\|_2$
0.5	0.0102	0.1392
2.5	0.0216	0.2401
$\epsilon = 0.04$		

t	$\|E\|_\infty$	$\|E\|_2$
0.5	0.0156	0.2638
2.5	0.0315	0.3920
$\epsilon = 0.08$		

Table 2: Error norms in Example 1, stochastic case

where $C_i \in [-L, L]$, and α_i, γ_i, are given positive numbers, $i = 1, ..., n$.

As the initial condition in use, we take the two-dimensional zero function, that is,

$$U(x, y, 0) \equiv 0.$$

We carry out a set of numerical experiments as explained below.

In each of them, we have a certain sequence of external stimuli, and simulate three different scenarios: $\epsilon = 0$ (deterministic case), $\epsilon = 0.04$ (weak noise) and $\epsilon = 0.08$ (strong noise). When the stochastic equation is simulated, we perform $ns = 100$ Monte Carlo runs and display their average value (as an approximation of the mathematical expectation of the solution). In certain cases that will be specified below, we increase this number to $ns = 500$. In all our examples (except in situations where other values are indicated), the space domain in use is $[-20, 20] \times [-20, 20]$ but our computation results are exposed for its half $[0, 20] \times [-20, 20]$, due to the physical meaning of the solution. The step size in time is $h_t = 0.1$, the step size in space is $h_x = h_y = 0.04$ and $K = 50$, that is, the number of basis functions is $51 \times 51 = 2601$.

4.1. Example 1

In this example, the external input consists of the traveling wave I_0 described by (24) and the localized signal I_1 of the type (25), which are constant during the time interval $t \in [0, 1.5]$ and, then, vanish. Their prefixed parameters are: $\alpha_0 = 0.12$, $\gamma_0 = 1$, $v = 1.5$; $\alpha_1 = 0.12$, $\gamma_1 = 1$, $C_1 = 0$. The threshold for the activation function S is $b = 0.1$ and the connectivity kernel is given by (23), with the constants $A = 0.06, l = 0.8, a_1 = 1$.

We begin at our assessment of the accuracy of the numerical method presented in section 3. With this purpose in mind, we estimate the absolute error of the lower order solution as the difference between the outcomes of the two above numerical integration techniques grounded in the Euler-Maruyama and Itô-Taylor discretization schemes). The norms of this error ($\|E\|_\infty$ and $\|E\|_2$) are given in Table 1 (deterministic case) and Table 2 (stochastic case) at $t = 0.5$ and $t = 2.5$. The norms of the solution are also displayed for comparison. In the deterministic case, the ratio $\|E\|_\infty / \|U\|_\infty$ (relative error) increases from about 0.06 (at $t = 0.5$) to 0.13 (at $t = 2.5$). In the stochastic case, this ratio grows in line with the disturbance level ϵ, as it could be expected. However it does not increase so fast in line with the time (when compared with the deterministic scenario).

τ	$\|E\|_\infty$	$\|E\|_2$
0.1	0.0056	0.0737
0.05	0.0028	0.0363
0.025	0.0014	0.0180

Table 3: Error norms in Example 1, at $t = 0.5$, in the deterministic case.

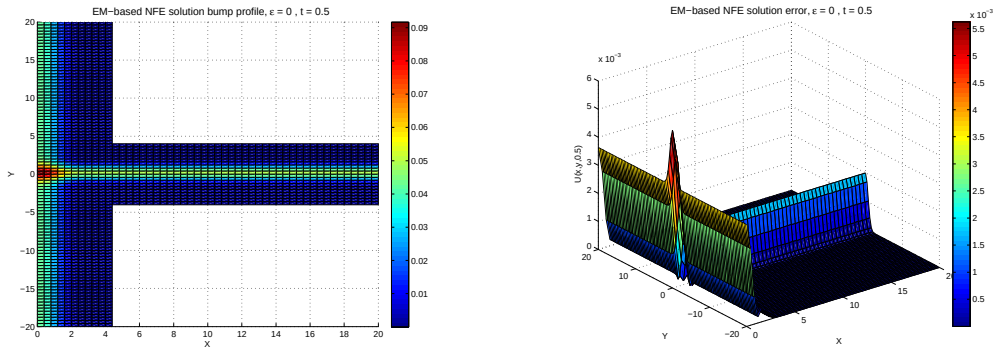

Figure 7: Graphs of Example 1 (deterministic case) at time $t = 0.5$: left-hand - solution; right-hand - error.

Fig. 7 illustrates the numerical solution calculated at $t = 0.5$ (while the external signal is active). Its left- and right-hand plots obtained by the lower order method and the corresponding error in the maximum norm, respectively. Similar plots for the solution yielded at $t = 2.5$ are depicted in Fig. 8.

Now we check the convergence order of the method, as h_t tends to 0. The dependence of the error norms on the step size h_t is presented in Tab. 4 . In this case, the Euler-Maruyama method in use reduces to the classical Euler method and the numerical results confirm the first order of convergence of the latter technique.

We further focus on the physical meaning of our numerical simulations. The physical interpretation of the input I_1 is a light signal of one color (with its coordinate $C_1 = 0$), which is turned off at time instant $t = 1.5$. We expect that the resulting neuronal activity reflects the properties of this signal.

At $t = 0.5$, as it could be expected, the neuronal activity is still subthreshold in the whole domain and reflects both the traveling wave I_0 and the localized signal I_1. At $t = 2.5$ (after the signal I_1 has been turned off), the solution is close to the stationary one and features one set where its value is suprathreshold. Its location reflects the color and the time of this light signal.

Next, we intend at studying the influence of random disturbance on the neural field under consideration.

In Fig. 9, the graphs of the numerical solution computed at time $t = 0.5$ are displayed for the noise levels $\epsilon = 0.04$ (left-hand) and $\epsilon = 0.08$ (right-hand). In both cases, we exhibit the mathematical expectation of the outcome solution, as explained above.

We see that, even in the case of the strong noise ($\epsilon = 0.08$), the structure of this solution is not essentially corrupted and it reflects adequately the features of the external input implemented.

Similar graphs observed at the time instant $t = 2.5$ are depicted in Fig. 10. Here, we see that

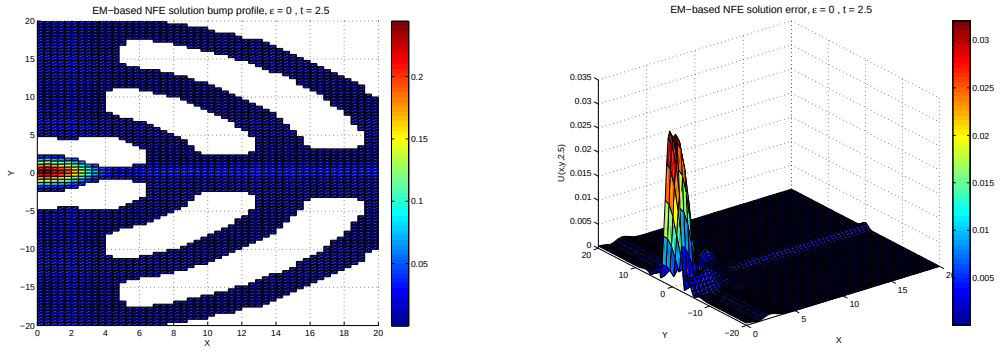

Figure 8: Graphs of Example 1 (deterministic case) at time $t = 2.5$: left-hand - solution; right-hand - error.

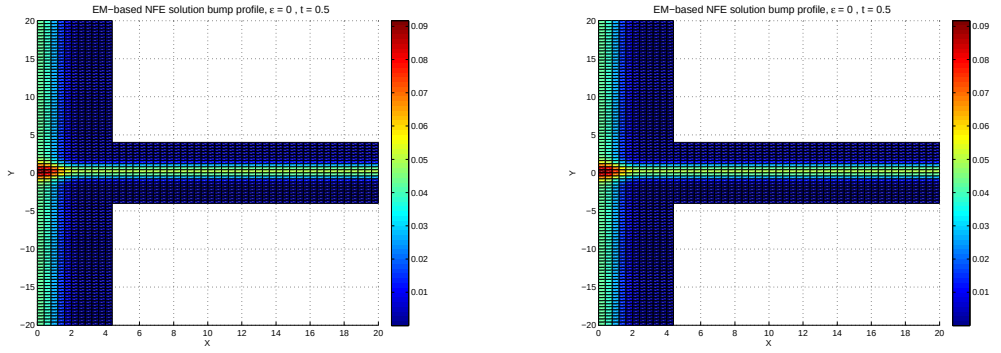

Figure 9: Graphs of Example 1 (deterministic case) at time $t = 0.5$: left-hand - solution; right-hand - error.

the structure of the solution does not change in comparison with the deterministic case. Moreover, we remark that the suprathreshold activity is concentrated within a certain space domain.

4.2. Example 2

In this case, we have again the traveling wave I_0 and two localized inputs I_1 and I_2 with $\alpha_1 = 0.12$, $\gamma_1 = 1$, $C_1 = -10$ and $\alpha_2 = 0.12$, $\gamma_2 = 1$, $C_2 = 10$, which correspond to the experiment with two different colors. As in the previous example, the inputs I_0, I_1 and I_2 are constant in the time interval $0 < t < 1$, and, then, are removed. The other parameters have the same values as those explained above.

Following this experimentation setup, we start our accuracy assessment of the lower-order method. In Tab. 4, the absolute error of the solution calculated at two time instants $t = 1$, $t = 5$ and in two different norms ($\|E\|_\infty$ and $\|E\|_2$) is exhibited. The norms of the solution yielded by the Euler-Maruyama-based approximation are also exposed for comparison. In the deterministic case, the relative error decreases from 0.13 (at $t = 1$) to 0.082 (at $t = 5$).

The errors in the stochastic scenario are displayed in Tab. 5. In the the case of the noise level $\epsilon = 0.04$, it decreases in time. In contrast, it slightly increases if $\epsilon = 0.08$. Looking closer at the error distribution, we observe that the maximum of the absolute error is attained at the same points of local maxima of the lower order numerical solution. However, the effect observed

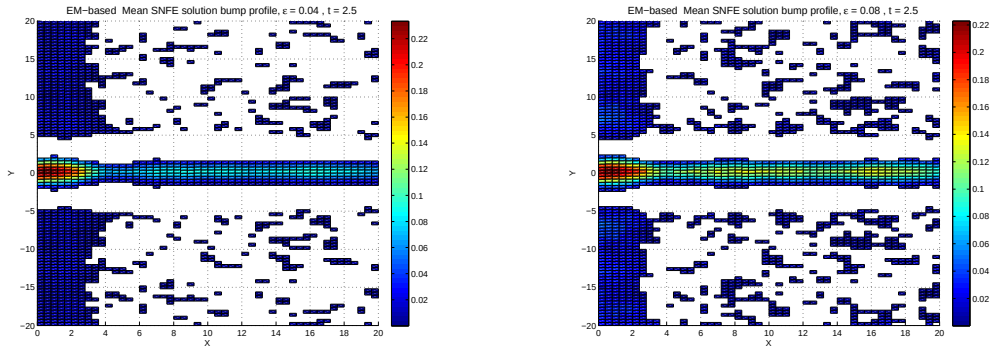

Figure 10: Graphs of Example 1 (stochastic case) at time $t = 2.5$: left-hand - $\epsilon = 0.04$; right-hand - $\epsilon = 0.08$.

t	$\|E\|_\infty$	$\|U\|_\infty$	$\|E\|_2$	$\|U\|_2$
1	0.0207	0.1804	0.1388	2.0527
5	0.0209	0.2554	0.1742	1.6043

Table 4: Error norm in Example 2, deterministic case.

disappears in the numerical solution calculated by our more accurate SNFE integration technique presented in section 3.3. This suggests that these local maxima are just an effect of the large discretization error committed by the Euler-Maruyama discretization scheme. The following step is to analyse and confirm numerically the convergence rate of our lower order approximation scheme, both in the deterministic scenario and in the stochastic one. For analysing the convergence in the stochastic case, we perform 500 Monte Carlo runs (because when $ns = 100$ the difference between the average numerical solution and its mathematical expectation is greater than the discretisation error committed). The error norms of the deterministic solutions derived with the decreasing step size $h_t = 0.2, 0.1, 0.05$, at the time instant $t = 1$ are displayed in Tab. 6. In line with Example 1, these numerical results confirm first order convergence our our numerical method described in section 3.2, as h_t tends to zero.

In Tab. 7 and Tab. 8, we analyze how the error norms derived for the numerical solutions calculated at the time instant $t = 1$ depend on the discretization step size h_t when $\epsilon = 0.04$ and $\epsilon = 0.08$, respectively. In both cases, the errors committed decrease in line with the size h_t of the equidistant mesh employed, though not so fast as in the deterministic case."The latter is quite clear and follows from the fact that the strong convergence order of the Euler-Maruyama approximation is only 0.5 in stochastic settings (see further details and explanation in [15, section 10.2]).

In this example, the physical interpretation of the external input $I_1 + I_2$ is a light signal of

t	$\|E\|_\infty$	$\|E\|_2$
1	0.0213	0.2147
5	0.0160	0.2029

$\epsilon = 0.04$

t	$\|E\|_\infty$	$\|E\|_2$
1	0.0233	0.3678
5	0.0360	0.4879

$\epsilon = 0.08$

Table 5: Error norms in Example 2, stochastic case.

h_t	$\|E\|_\infty$	$\|E\|_2$
0.2	0.0395	0.2638
0.1	0.0207	0.1388
0.05	0.0104	0.0662

Table 6: Error norms in Example 2, at $t = 1$, in the deterministic case.

h_t	$\|E\|_\infty$	$\|E\|_2$
0.2	0.0207	0.2974
0.1	0.0169	0.1871
0.05	0.0095	0.1546

Table 7: Error norms in Example 2, at $t = 1$, for three different meshes, in the case $\epsilon = 0.04$.

two colors (with their coordinates $C_1 = -10$ and $C_2 = 10$), which is turned off at the time instant $t = 1.0$. We further investigate how the neuronal activity reflects the properties of this signal.

We start by considering the deterministic scenario ($\epsilon = 0$). In this case, we perform numerical experiments by applying both solution methods presented in section 3 in the time interval $[0, 5]$.

Fig. 11 illustrates the solution computed at $t = 1$ (the last moment when the signal is active). The left and right-hand plot display the solution obtained by the lower order method and the corresponding error committed, respectively.

Similar plots for the solution yielded at the time instant $t = 5$ are depicted in Fig. 12.

At $t = 1$, the neuronal activity reflects both the traveling wave I_0 and the localized signals I_1 and I_2. This solution takes its maximal values at the places where the graphic of the traveling wave I_0 overlaps those of the external inputs I_1 and I_2.

At $t = 5$ (after the signal has been turned off), there exist two space domains where the solution takes suprathreshold values. Their locations reflect the colors and the time of these light signals.

Now we analyse how the numerical solution derived is affected by the random disturbance utilized in Example 2.

In Fig. 13, the graphs of the mean solutions computed by the numerical method in use at the time instant $t = 1$ are displayed in our stochastic scenarios with the noise levels $\epsilon = 0.04$ (left) and $\epsilon = 0.08$ (right). At this moment of time, the noise does not strongly change the main features of the solution.

Similar graphs reflecting the solution's behavior at the time instant $t = 5$ are depicted in Fig. 14. Here, we see that the structure of the solution yielded in our stochastic scenario with $\epsilon = 0.04$ does not change in comparison with the deterministic case. Furthermore, we remark that the suprathreshold activity is concentrated within two particular space domains. However, in the

h_t	$\|E\|_\infty$	$\|E\|_2$
0.2	0.0249	0.3926
0.1	0.0218	0.3106
0.05	0.0166	0.2918

Table 8: Error norms in Example 2, at $t = 1$, for three different meshes, in the case $\epsilon = 0.08$.

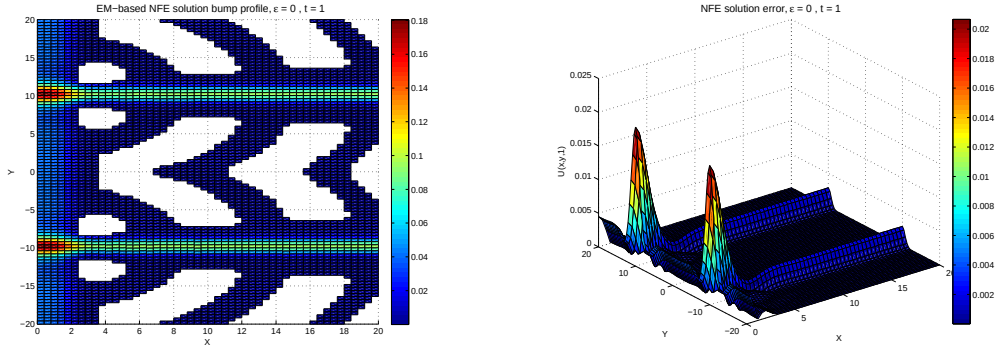

Figure 11: Graphs of Example 2 (deterministic case) at time $t = 1$: left-hand - solution; right-hand - error.

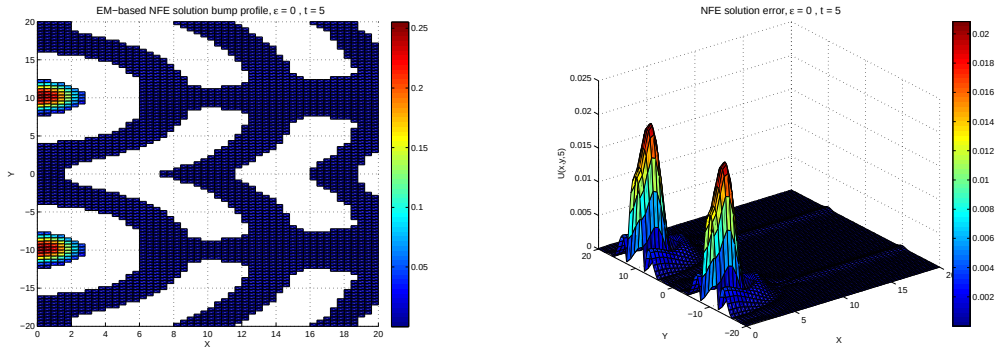

Figure 12: Graphs of Example 2 (deterministic case) at time $t = 5$: left-hand - solution; right-hand - error.

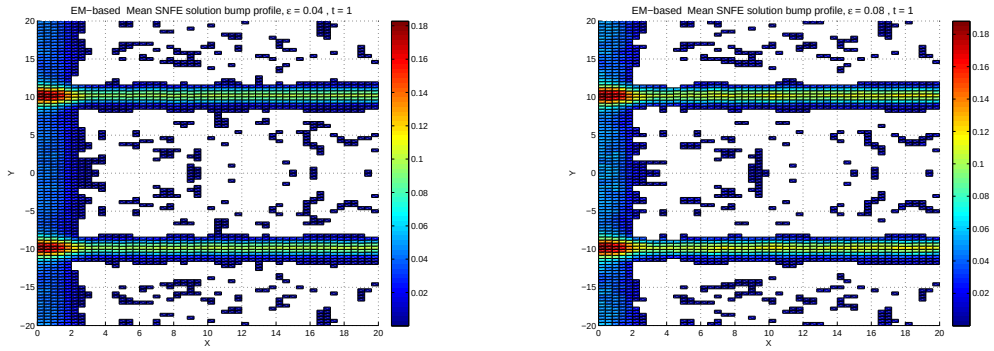

Figure 13: Graphs of Example 2 (stochastic case) at time $t = 1$: left-hand - solution; right-hand - error.

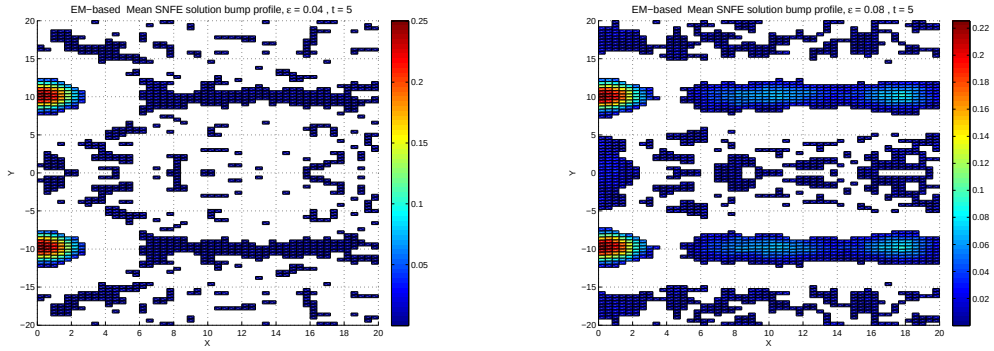

Figure 14: Graphs of Example 2 (stochastic case) at time $t = 5$: left-hand - $\epsilon = 0.04$; right-hand - $\epsilon = 0.08$

stochastic scenario with the noise level $\epsilon = 0.08$, our lower order method produces the numerical solution whose local maxima are observed at the positions with their coordinates close to $x = 18$, $y = 10$ and $x = 18$, $y = -10$. These become indistinguishable in the scenarios where the random disturbance is either $\epsilon = 0.04$ or $\epsilon = 0$.

4.3. Example 3

In this experiment, we have three series of inputs at different times. First, in the time interval $[0, 1]$, we employ I_0, I_1 and I_2 (with the same parameters as in Example 2). Second, in $[1, 5]$, we implement only the traveling wave I_0. Third, in the time interval $[5, 6]$, we have I_0, I_3 and I_4 where $I_3 = 1.2\, I_1$ and $I_4 = 1.2\, I_2$. After $t = 6$, all the inputs are canceled.

Concerning the accuracy of the numerical results, Tabs 9 and 10 show how the error norms of the lower order solution, that is, ($\|E\|_\infty$ and $\|E\|_2$), depend on t when $\epsilon = 0, 0.04$ and 0.08, respectively. In Tab. 9, the mentioned norms of the solution itself are also displayed for comparison. In the deterministic case, the relative error increases from 0.12 (at $t = 1$) to 0.28 (at $t = 8$). In the stochastic case (both for $\epsilon = 0.04$ and $\epsilon = 0.08$), the relative error decreases in time.

Now we focus on the physical interpretation of this numerical experiment. In our scenario, the external input $I_1 + I_2$ corresponds to a light signal of two colors (with their coordinates $C_1 = -10$

t	$\|E\|_\infty$	$\|U\|_\infty$	$\|E\|_2$	$\|U\|_2$
1	0.0177	0.1435	0.1134	1.7439
6	0.0697	0.3477	0.5605	2.9178
8	0.0805	0.2844	0.7524	2.4414

Table 9: Error norms in Example 3, deterministic case.

t	$\|E\|_\infty$	$\|E\|_2$
1	0.0191	0.1984
6	0.0236	0.2694
8	0.0225	0.3026

$a)\epsilon = 0.04$

t	$\|E\|_\infty$	$\|E\|_2$
1	0.0221	0.3556
6	0.0314	0.4797
8	0.0274	0.5082

$b)\epsilon = 0.08$

Table 10: Error norms in Example 3, stochastic case.

and $C_2 = 10$), which is turned off at the time instant $t = 1.0$. Then, the external input $I_3 + I_4$ describes another light signal of two colors, which is active in the time interval $[5, 6]$.

Again, we begin at the deterministic case. As in the previous examples, we perform numerical experiments by applying our both solution methods presented in section 3 in the time interval $[0, 8]$.

At $t = 1$, the behavior of the solution derived is almost identical to that calculated in Example 2. So, we do not plot it explicitly, here.

Plots of the solution and its error yielded at the time instant $t = 6$ are depicted in Fig. 15.

At $t = 6$, as an effect of the signal $I_3 + I_4$, two additional bumps appear in this figure in comparison to the similar result computed in Example 2.

Finally, the numerical solution realized at $t = 8$ implements the full account of the external input signals applied. The graph of this solution and its error committed are depicted in Fig.16.

As it could be expected, the graph of the solution contains four bumps. Among them, two correspond to the first light signal and the remaining bumps stem from the second one.

Next, we aim at exploring the effect of noise in Example 3. The graphs of the solution computed by the numerical method in use at the time instant $t = 6$ in our stochastic scenarios with the random

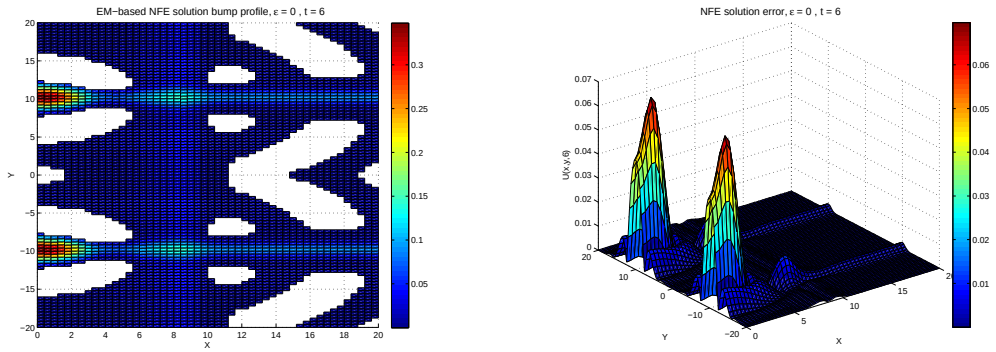

Figure 15: Graphs of Example 3 (deterministic case) at time $t = 6$: left-hand - solution; right-hand - error.

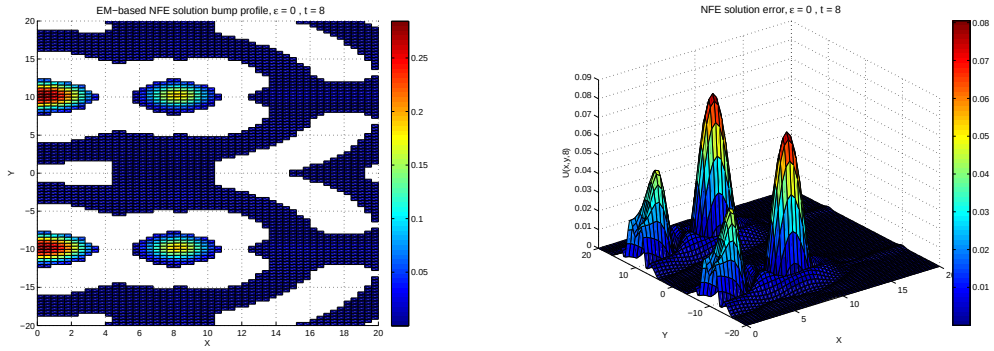

Figure 16: Graphs of Example 3 (deterministic case) at time $t = 8$: left-hand - solution; right-hand - error.

disturbance levels $\epsilon = 0.04$ (left) and $\epsilon = 0.08$ (right) are displayed in Fig. 17. In Fig. 18, similar graphs are exhibited for the time instant $t = 8$.

In the case of the strong noise (with the disturbance level $\epsilon = 0.08$), Fig.18 shows an interesting feature, which is not observed in the previous examples. Instead of 4 bumps, that might be expected in this situation, the field activity contains 6 ones, that is, two additional bumps have been formed just as an effect of the implemented random disturbance. Note that this happens neither in the deterministic case nor in the case of the weak noise.

In order to observe how this picture changes in time, we extend our computations to the longer time interval $[0, 15]$. Then, we observe that these two additional bumps arisen in the strong noise scenario with $\epsilon = 0.08$ do not vanish or even decrease in time. Moreover, we remark that this behavior observed in our calculation does not depend on the numerical methods employed, that is, the numerical solutions yielded by the lower and higher order methods presented in section 3 expose the same phenomenon. Therefore this is hardly an implication of the error committed, but rather an effect of the noise implemented.

Here, we also encounter the phenomenon of false memories, which can be induced by random disturbance. Differently from the input-induced bumps, their activity level is subthreshold, that is, less than $b = 0.1$. Such an observation can be explained as follows: only part of the paths of the sampled numerical solutions contain these two additional bumps (whose height should be above the suprathreshold value), while the remaining ones are similar to those shown in the deterministic solution. Since what we show in the picture is the sample mean solution, the heights of these bumps are averaged on all the paths computed and, hence, they are subthreshold.

It is also worth to mention that the distance between a "false" bump and the closest real memory representation is approximately the coordinate of one of the local maxima of the connectivity function, that is, the location of this false memory receives the excitation from the existing bumps.

4.4. Example 4

In this experiment, we implement three series of external stimuli at different times.

First, in the time interval $[0, 1.5]$, we employ I_0 and I_1; here, I_1 is the localized input defined in Example 1 (that is, $\alpha_0 = 0.12$, $\gamma_0 = 1$, $v = 1.5$; $\alpha_1 = 0.12$, $\gamma_1 = 1$, $C_1 = 0$). Then, in the subsequent time interval $[1.5, 3]$, we utlize only the traveling wave I_0. Finally, in the time interval

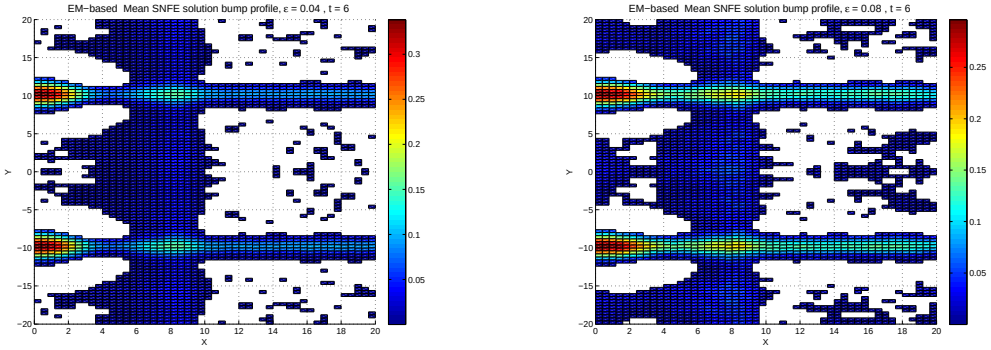

Figure 17: Graphs of Example 3 (stochastic case) at time $t = 6$: left-hand - $\epsilon = 0.04$; right-hand - $\epsilon = 0.08$.

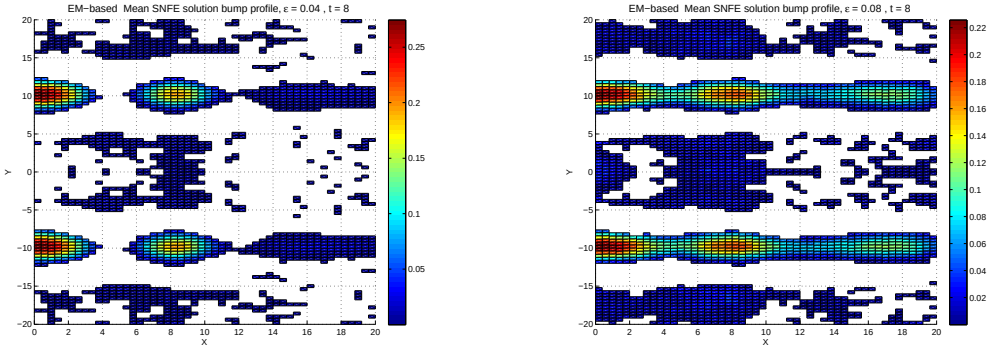

Figure 18: Graphs of Example 3 (stochastic case) at time $t = 8$: left-hand side - $\epsilon = 0.04$; right-hand side - $\epsilon = 0.08$.

t	$\|E\|_\infty$	$\|U\|_\infty$	$\|E\|_2$	$\|U\|_2$
1	0.0177	0.1435	0.0926	1.3603
4	0.0448	0.2462	0.2808	2.1495
7	0.0251	0.2558	0.2041	2.2765

Table 11: Error norms in Example 4, deterministic case.

t	$\|E\|_\infty$	$\|E\|_2$
1	0.0165	0.1824
4	0.0225	0.2750
7	0.0354	0.3608

$\epsilon = 0.04$

	$\|E\|_\infty$	$\|E\|_2$
1	0.0220	0.3375
4	0.0241	0.4422
7	0.0465	0.5507

$\epsilon = 0.08$

Table 12: Error norms in Example 4, stochastic case.

$[3, 4.5]$, we apply the stimulus signals I_0, I_3 and I_4 where I_3 and I_4 are defined precisely as those in Example 3. After $t = 4.5$, all the above inputs are removed.

As usual, I_1 corresponds to a light signal of one color. Then, the sum $I_3 + I_4$ simulates a light signal of two colors, which is active in the time interval $[3, 4.5]$.

As in the other numerical examples, we begin by analysing the error norms of the solution computed by the numerical methods presented in section 3 at different time instants.

The error norms of the solution derived within our deterministic and stochastic scenarios at the time instants $t = 1$, $t = 4$ and $t = 7$ are displayed in Tabs. 11 and 12, respectively. While in the deterministic case the error norms increase from $t = 1$ to $t = 4$ and, then, decrease from $t = 4$ to $t = 7$, in the stochastic simulations the error norms of the solution computed increase monotonically in time.

For addressing the physical meaning of this numerical simulation, we begin at a consideration of the deterministic case. As in the previous examples, we perform numerical experiments by applying both solution methods presented in section 3 in the time interval $[0, 7]$.

For $t < 3$, the behavior of the solution derived is almost identical to that calculated in Example 1. So, we do not plot it explicitly, here.

Plots of the solution and its error yielded at the time instant $t = 4$ are depicted in Fig. 19.

At $t = 4$ (when the input $I_3 + I_4$ is active), two additional bumps appear in this figure in comparison to the similar result computed in Example 1. These stem from the new signal applied to our 2D-SNFE model under consideration

Finally, the numerical solution realized at $t = 7$ implements the full account of the externals input signals applied. The graph of this solution and its error committed are depicted in Fig.20.

As it could be expected, the graph of the numerical solution under study contains three bumps. Among them, one corresponds to the first light signal and the remaining bumps stem from the second one.

As in the previous example, the random disturbance implemented may cause important changes in the output of this simulation. The graphs of the solutions computed by the numerical method in use at the time instant $t = 4$ are displayed in Fig. 21 in the cases of $\epsilon = 0.04$ (left) and $\epsilon = 0.08$ (right). In Fig. 22, similar data are exhibited for the time instant $t = 7$.

In the case of the weak noise, that is, with the disturbance level $\epsilon = 0.04$, the average sample

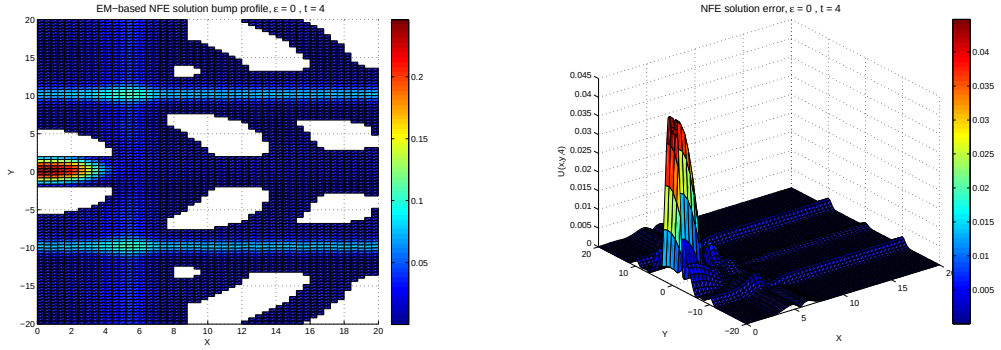

Figure 19: Graphs of Example 4 (deterministic case) at time $t = 4$: left-hand - solution ; right-hand - error.

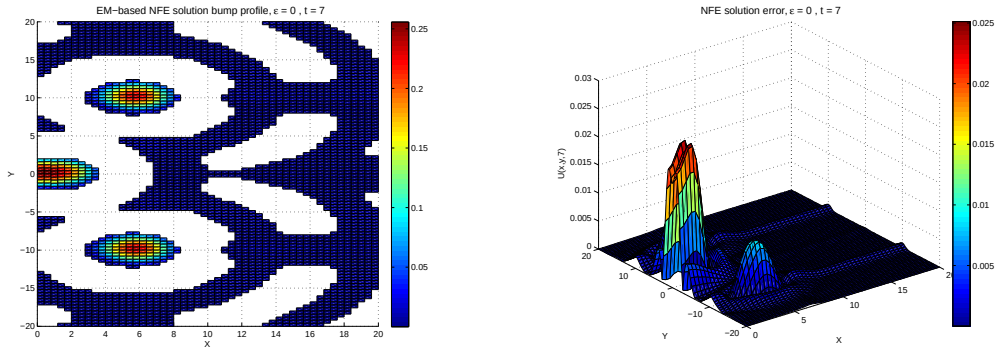

Figure 20: Graphs of Example 4 (deterministic case) at time $t = 7$: left-hand - solution ; right-hand - error.

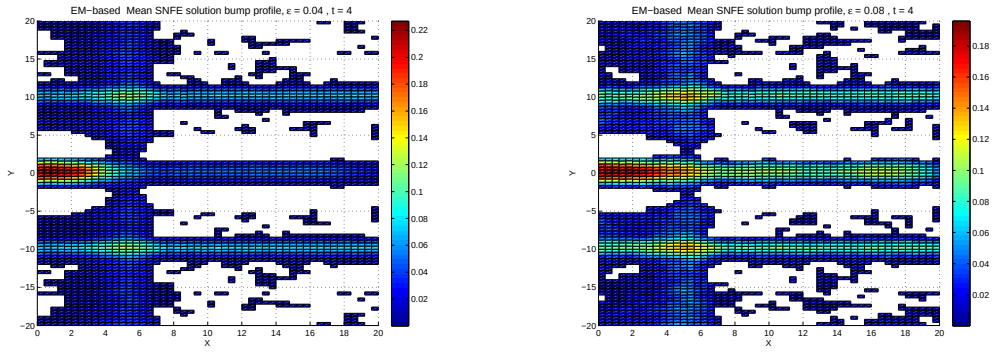

Figure 21: Graphs of Example 4 (stochastic case) at time $t = 4$: left-hand - $\epsilon = 0.04$; right-hand - $\epsilon = 0.08$.

act. zones	1	2	3	4
$\epsilon = 0.04$	48	50	2	0
$\epsilon = 0.08$	7	41	50	2

a)Euler-Maruyama approximation;

act. zones	1	2	3	4
$\epsilon = 0.04$	74	26	0	0
$\epsilon = 0.08$	10	48	38	4

b) Itô-Taylor approximation.

Table 13: distribution of the solution paths according to the number of activity zones that can be found on the line $y = 0$, at $t = 7$.

solution at $t = 7$ has 3 bumps, that is, as much as the deterministic numerical solution has. However, in the case of the disturbance level $\epsilon = 0.08$, the average sample solution possesses 8 bumps, that is, 5 additional bumps appear as a result of this random disturbance. Among them, two have their maxima at $y = 10$, other two at $y = -10$ and the remaining one at $y = 0$. As in Example 3, the solution values at these points do not exceed the level $b = 0.1$ (as it happens usually in the bumps arisen in the deterministic case).

For a deeper investigation of this phenomenon, we pay attention to the behavior of separate paths of our stochastic solution. More precisely, in the output of each Monte Carlo run, we consider three parallel lines with coordinates $y = -10$, $y = 0$ and $y = 10$, and count the particular solution's intersections with the threshold $b = 0.1$. Dividing this quantity by 2, we obtain the number of activity zones under consideration along these lines. We choose the above mentioned values of y because, as the average sample solution predicts, these are the coordinates where such additional bumps are likely to appear.

In Tab.13, we show the distribution of the solution paths according to the number of activity zones that are found along the line with coordinate $y = 0$,for two different levels of simulated noise ($\epsilon = 0.04$ and $\epsilon = 0.08$) at the time instant $t = 7$. In the case of $\epsilon = 0.04$, we observe that the large majority of the 100 paths sampled has only one activity zone. However, when $\epsilon = 0.08$ most of the solution paths has 2 or 3 activity zones (and some have even four zones). We emphasize that the conclusion derived stays true for both numerical solutions yielded by the lower and higher order methods presented in section 3. Concerning the lines with the coordinates $y = 10$ and $y = -10$, the picture is similar. Eventually, the formation of "false" bumps is typical in the stochastic scenario with the disturbance level $\epsilon = 0.08$ but occurs rarely when $\epsilon = 0.04$.

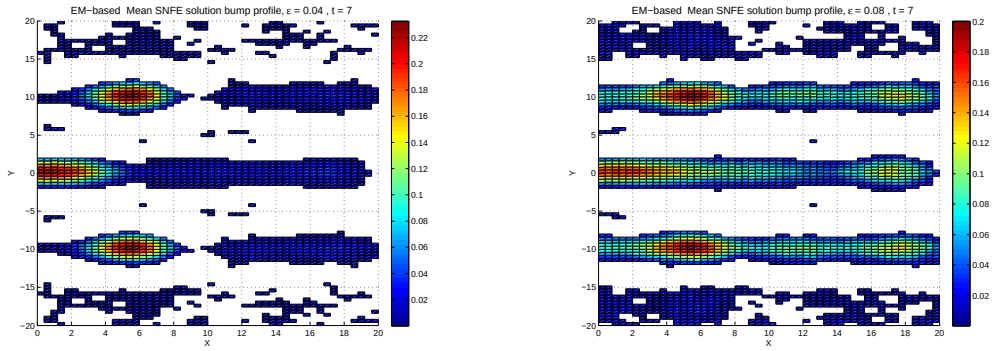

Figure 22: Graphs of Example 4 (stochastic case)at time $t = 7$: left-hand - $\epsilon = 0.04$; right-hand - $\epsilon = 0.08$.

5. Conclusion

In what concerns the physical interpretation of the numerical results, the main finding of this work is that we can explain the evolution of neurons tuned to a specific point in time using the wave mechanism. What is important here is the fact that the bumps reflect the memory of a certain color event at a certain time after a sequence onset at $t = 0$.

There is a linear dependence between the location of the bumps in the x-direction of the field and the time interval when the corresponding stimulus is active.

For instance, in Example 3 the series of external stimuli is applied in the time interval $[5, 6]$ and the bases of the corresponding bumps are located approximately in the interval $[6.5, 9]$ (see, for example, Fig. 16).

If instead of our assumption in Sec. 4.3 we suppose now that the third series of stimuli is applied during the time interval $[6, 7]$ we observe that bumps appear to be shifted to the interval $[8, 11]$.

Moreover, in Example 4, the time interval of the third series of inputs is $[3, 4.5]$ and the bases of the corresponding bumps are located approximately in the interval $[4, 7]$ of the x-axis (see Fig. 20). When the time interval of the mentioned inputs is changed to $[4.5, 6]$, the bases of the corresponding bumps move to the interval $[5, 9]$ of the x-axis.

It is also remarkable that the width of the bumps in the x-direction is nearly proportional to the duration of the external stimuli (in Example 4, this width is larger than in Example 3, where the time intervals are shorter).

The linear dependence between the coordinates of the bumps in the x-direction of the neural field and the time intervals is determined by the propagation speed v of the traveling wave I_0 described by formula (24). In our numerical experiments, we have considered $v = 1.5$. In the case of a different propagation speed, the coordinates of the bumps are different, but still proportional to the time intervals defined by the input events. This result suggests that the wave mechanism is consistent with experimental findings of a scalable neural population code for time [28].

In applications of dynamic field models [7, 32], the read-out of the stored information is typically performed by applying the stable multi-bump pattern as a subthreshold input to a decision field. For the present application, when at the time of sequence recall the same additional wave input is applied to this field as during the encoding phase, bumps representing individual color events will evolve in the correct sequential order. However, their temporal evolution will be systematically

delayed by a certain time interval since the memory bumps are not centered at the correct position. An additional neural calibration process is needed that uses the temporal mismatch between the expected and the predicted timing of the first sequence event to adjust the wave velocity accordingly. It should be noted however that many experiments in the domain of temporal cognition [27] show that our subjective time perception is prone to distortions depending on the influences of many factors including the presence of additional items in working memory.

Another important fact confirmed by our experiments is that the coordinates of the bumps representing the events are not strongly affected by noise, neither in the x nor in the y direction. In Figs. 18 and 22, we observe that, even in the case of $\epsilon = 0.08$ (strong noise), the location of the bumps does not differ significantly from their location in the deterministic case (compare with Figs. 16 and 20, respectively).

On the other hand, the combined effect of noise and connectivity between neurons may lead to the formation of bumps that are independent of the external inputs. This is clearly visible both in Example 3 (Fig. 18) and Example 4 (Fig. 22).

Looking at Fig. 16 (case $\epsilon = 0$), we observe blue circular rings surrounding the bumps. The distances between these rings and the centers of the bumps is close to 6, which corresponds to one of the local maxima of the connectivity function $F(r)$, as follows from equation (23). We can therefore conclude that these rings represent zones of subthreshold activity, which result from the excitation received from the bumps. Moreover, we observe blue strips, situated approximately at $y = 10$ and $y = -10$. These correspond to subthreshold activity, resulting from the external inputs I_3 and I_4. Eventually, it is not surprising that the additional bumps arising in the case of $\epsilon = 0.08$ (Fig. 18, right-hand plot) are located approximately at the intersection of the blue rings and strips of Fig.16. Such intersections represent the regions of the greatest subthreshold activity in the deterministic case, where new bumps are likely to appear under the effect of noise.

A similar explanation can be given to the location of the additional bumps arisen in the presence of the random disturbance in Example 4. In this case, we just have to compare Fig. 20 (left-hand plot) with Fig. 22 (right-hand plot).

The other important outcome of this work is the assessment of the accuracy and robustness of the computational algorithm used for the numerical simulations. The combination of two methods of different convergence orders (Euler-Maruyama and Itô-Taylor) described in Sec. 3 has proved to be an efficient way for controlling the computational error and increasing the accuracy of the obtained numerical results.

A limitation of the presented numerical method is its restriction that the solution should be an even function with respect to both spatial variables. It follows from the choice of the basis functions (4) in use. A possible direction for improving this algorithm is to consider basis functions of a more general form, which will enable us simulate neural fields with different types of symmetry. Concerning future work, we also plan to apply the same computational algorithm for analyzing different configurations of external stimuli. In particular, we intend to study distance-dependent spatial attraction and repulsion effects between input-induced bumps that may cause memory distortions [1, 9]. Such effects arise from the existence of lateral excitation and inhibition in the type of network connectivity described by the function $F(r)$. With this investigation, we aim at further exploring the advantages and challenges of employing dynamic neural fields to simulate joint order and timing representations of working memory.

6. Acknowledgements

The authors acknowledge the financial support of the Portuguese FCT (Fundação para a Ciência e Tecnologia) , through projects UIDB/04621/2020, UIDP/04621/2020 (IST), UIDB/00013/2020, UIDP/00013/2020 (UMinho) and PTDC/MAT-APL/31393/2017. The authors are also grateful to the reviewers for their careful reading of the text and helpful suggestions that contributed to the improvement of the article.

References

[1] Amari S.L., Dynamics of pattern formation in lateral-inhibition type neural fields, Biol. Cybernet. **27** (2) 77–87 (1977).

[2] Bressloff P. C., Spatiotemporal dynamics of continuum neural fields. Journal of Physics A: Mathematical and Theoretical, **45**(3), 033001 (2011).

[3] Coombes S., beim Graben P., Potthast R., and Wright J., Neural Fields. Springer Berlin, Heidelberg, 2014 .

[4] Coombes S., Large-scale neural dynamics, Simple and complex, NeuroImage **52**, 731–739 (2010).

[5] Curtis C., and Lee, D., Beyond working memory: the role of persistent activity in decision making, Trends in cognitive sciences **14** (5), 216–222 (2010).

[6] Erlhagen W. , Bastian A., Jancke D., Riehle A, and Schoner G., The distribution of neuronal population activation (DPA) as a tool to study interaction and integration in cortical representations, Journal of Neuroscience Methods **94** , 1, 53–66 (1999).

[7] Erlhagen W., and Bicho E., The dynamic neural field approach to cognitive robotics, Journal of Neural Engineering **3**,3, R36 (2006).

[8] Faye G. and Faugeras O., Some theoretical and numerical results for delayed neural field equations, Physica D **239** 561–578 (2010).

[9] Ferreira F. , Erlhagen W., and Bicho E., Multi-bump solutions in a neural field model with external inputs, Physica D: Nonlinear Phenomena, **326**, 32–51 (2016).

[10] Ferreira F., Wojtak W., Sousa E., Louro L., Bicho, E., and Erlhagen, W., Rapid learning of complex sequences with time constraints: A dynamic neural field model, IEEE Transactions on Cognitive and Developmental Systems (2020).

[11] Guo Y., and Chow C. C.,Existence and stability of standing pulses in neural networks: II. Stability. SIAM Journal on Applied Dynamical Systems,**4** (2), 249-281 (2005).

[12] Hutt A. and Rougier N., Activity spread and breathers induced by finite transmission speeds in two-dimensional neuronal fields, Physical Review,E **82** 055701 (2010).

[13] Hutt A. and Rougier N., Numerical simulations of one- and two-dimensional neural fields involving space-dependent delays. In: S. Coombes et al. (Eds.), Neural Fields Theory and Applications, 175–183, Springer (2014).

[14] Kilpatrick Z. and Ermentrout B., Wandering bumps in stochastic neural fields, SIAM J. Appl. Dyn. Syst., **12** 61–94 (2013).

[15] Kloeden, P. and Platen, E., *Numerical Solution of Stochastic Differential Equations*. Berlin: Springer (1999).

[16] Kühn, C. and Riedler M.G., Large deviations for nonlocal stochastic neural fields, J. Math. Neurosci. **4** ,1, 1–33 (2014).

[17] Kulikov G. Yu. , Lima P. M. , and Kulikova M.V., Numerical solution of the neural field equation in the presence of random disturbance. J. Comput. Appl. Math. **387**, 112563 (2021).

[18] Kulikova M.V., Kulikov G.Yu., and Lima P.M., Effective Numerical Solution to Two-Dimensional Stochastic Neural Field Equations.*Proceedings of the 23rd International Conference on System Theory, Control and Computing, ICSTCC 2019* 650-655 (2019).

[19] Kulikova M. V., Kulikov G. Yu., and Lima, P. M., Accuracy study in numerical simulations to stochastic neural field equations, *Proceedings of 2020 24th International Conference on System Theory, Control and Computing (ICSTCC 2020)* 254-261 (2020).

[20] Laing C. R., Troy W. C., Gutkin B. and Ermentrout G.B., Multiple bumps in a neuronal model of working memory, SIAM Journal on Applied Mathematics, **63**, 1, 62–97 (2002).

[21] Laing C. R., and Troy W. C., PDE methods for nonlocal models. SIAM Journal on Applied Dynamical Systems,**2**(3), 487-516 (2003).

[22] Lima P.M., and Erlhagen W., Numerical Simulations of Two-Dimensional Neural Fields with Applications to Working Memory *Proceedings of the 2018 European Control Conference, ECC 2018* 2040-2045 (2018).

[23] Lima, P.M. and Buckwar, E., Numerical solution of the neural field equation in the two-dimensional case, SIAM Journal of Scientific Computing, **37**, B962– B979 (2015).
[24] Lima P.M. and Buckwar E., Numerical investigation of the two-dimensional neural field equation with delay. In: Proceedings of the Second International Conference on Mathematics and Computers in Sciences and in Industry, 131 - -137, IEEE Conference Publications (2015).
[25] Lima P.M., Numerical Investigation of Stochastic Neural Field Equations, in Advances in Mathematical Methods and High Performance Computing: V.K. Sing , D. Gao, A. Fischer, Eds., 51-67 (2019). **24.3**, 242–258 (2020).
[26] Mechant et al., Interval tuning in the primate medial premotor cortex as a general timing mechanism, The Journal of Neuroscience **22** 9082–9096 (2013).
[27] Matthews W. and Meck W.H., Temporal cognition: connecting subjective time to perception, attention, and memory. Psychological bulletin, **142**, 865 (2016).
[28] Mello G., Soares S., and Paton, J., A scalable population code for time in the striatum, Current Biology, **25** (9), 1113–1122 (2015).
[29] Muller L., Chavane F., Reynolds J., and Sejnowski T.J., Cortical travelling waves: mechanisms and computational principles, Nature Reviews Neuroscience, **19**,5, 255-268 (2018)
[30] Pinto D. J., and Ermentrout G. B., Spatially structured activity in synaptically coupled neuronal networks: II. Lateral inhibition and standing pulses. SIAM Journal on Applied Mathematics, **62** (1), 226-243 (2001).
[31] Sandstede B., Evans functions and nonlinear stability of traveling waves in neuronal network models. International Journal of Bifurcation and Chaos, **17**(08), 2693–2704 (2007).
[32] Schöner G., and Spencer J., Dynamic thinking: A primer on dynamic field theory. Oxford University Press, 2015.
[33] Shardlow T., Numerical simulation of stochastic PDEs for excitable media, J. Comput. Appl. Math., **175**, 429–446 (2005).
[34] Sheretinsky A., Fundamentals of recurrent neural network (RNN) and long short-term memory (LSTM) network, Physica D: Nonlinear Phenomena, **404**, 132306 (2020).
[35] Wilson H.R. and Cowan J.D., Excitatory and inhibitory interactions in localized populations of model neurons, Bipophys. J., **12** 1–24 (1972).
[36] Wojtak W., Coombes S., Avitabile D., Bicho E., and Erlhagen W., A dynamic neural field model of continuous input integration, Biological Cybernetics **115** 451–471 (2021).
[37] Wojtak W., Ferreira F., Bicho E., and Erlhagen W., Neural field model for measuring and reproducing time intervals, in Artificial Networks and Machine Learning - ICANN2019: Theoretical Neural Computation, ed. by I.V.Tetko et al., Springer International Publishing, 2019 327–338.
[38] Wojtak W., Ferreira F., Vicente P., Louro L., Bicho E., and Erlhagen W., Neural integrator model for planning and value-based decision making of a robotics assistant, Neural Computing and Applications, 1 –20 (2020).